Rock Mechanics and Rock Engineering
https://doi.org/10.1007/s00603-018-1702-z

ORIGINAL PAPER

A Fundamental Investigation of the Tensile Failure of Rock Using the Three-Dimensional Lattice Spring Model

Qin Li[1] · Gao-Feng Zhao[1] · Jijian Lian[1]

Received: 13 June 2018 / Accepted: 11 November 2018

Abstract

A fundamental study on the tensile failure of rock is conducted using the three-dimensional lattice spring model. The model covers three aspects: (1) the relationship between the mesoscopic tensile/shear failure and the corresponding macroscopic tensile failure; (2) the effects of the size, shape, and location of the initial defect on the macroscopic tensile failure; and (3) the effects of the porosity, heterogeneity, crystal structure, mesoscopic constitutive model, and model scale on its macroscopic tensile responses. Through investigation, this study reveals that the mesoscopic strength heterogeneity affects the macroscopic pre-peak response of rock, and the initial defect could control its macroscopic post-peak response. The post-peak characteristics of the mesoscopic constitutive model influence both the macroscopic pre-peak and post-peak responses, which are scale independent and scale dependent, respectively. Based on these investigations, a parameter-selection method for the mesoscopic constitutive model is established to fully utilize the macroscopic tensile experimental data.

Keywords Lattice spring model · Tensile failure · Post-peak responses · Constitutive model · Scale effect

List of Symbols

Roman Alphabet

$D(\cdot)$	The damage amount of the spring bond
$D_{\mathrm{n}}(\cdot)$	The damage function of the normal spring
$D_{\mathrm{s}}(\cdot)$	The damage function of the shear spring
$f(\cdot)$	A mathematic function for damage description
$\mathbf{F}_{\mathrm{n},ij}$	The normal interaction forces (vectors)
$\mathbf{F}_{\mathrm{s},ij}$	The shear interaction forces (vectors)
k_{n}	The shiftiness of the normal spring
k_{s}	The shiftiness of the shear spring
$\overline{l}$	The mean length of the spring bond in the lattice model
l_i	The length of the i-th spring bond in the lattice model
m	A shape coefficient of the Weibull distribution
m_p	The particle mass
$\mathbf{n}$	The initial unit vector of the connected particles
$\mathbf{n}_s$	The direction unit vector of the tangential deformation of the spring bond
$\mathbf{u}_i$	The displacement of particle$i$
$\mathbf{u}_j$	The displacement of particle$j$
$\mathbf{u}_{\mathrm{n},ij}$	The relative normal deformation vector between particles
$\mathbf{u}_{\mathrm{s},ij}$	The relative tangential deformation vector between particles
$\dot{\mathbf{u}}$	The particle velocity
u_{n}	The normal deformations of the spring
u_{n}^*	The maximum tensile deformation of the spring
u_{s}	The tangential deformations of the spring
$\lvert u_{\mathrm{s}}\rvert$	The absolute value of the shear deformation
u_{s}^*	The maximum shear deformation of the spring
u^*	The ultimate deformation
u	The current deformation
υ	The Poisson's ratio
V	The represented macroscopic volume of the computational model
x	The non-dimensional spring deformation
x_i	The initial coordinate of particle i
y_i	The initial coordinate of particle i
z_i	The initial coordinate of particle i
x_j	The initial coordinate of particle j
y_j	The initial coordinate of particle j
z_j	The initial coordinate of particle j
Δt	The time step

✉ Jijian Lian
jjlian@tju.edu.cn

[1] State Key Laboratory of Hydraulic Engineering Simulation and Safety, School of Civil Engineering, Tianjin University, Tianjin, China

Published online: 19 January 2019

Greek Symbols

α	A non-dimensional parameter for the mesoscopic constitutive model
β	A parameter for the mesoscopic constitutive model
ζ	A random number that satisfies a certain distribution
ξ_i	The random number assigned to particle i
ξ_j	The random number assigned to particle j
ξ^{3D}	The lattice coefficient
$[\varepsilon]_{bond}$	The local strain of a spring bond
$\bar{\sigma}_t$	The macroscopic tensile strength
σ_t	The macroscopic tensile strength
λ	A scale increase factor

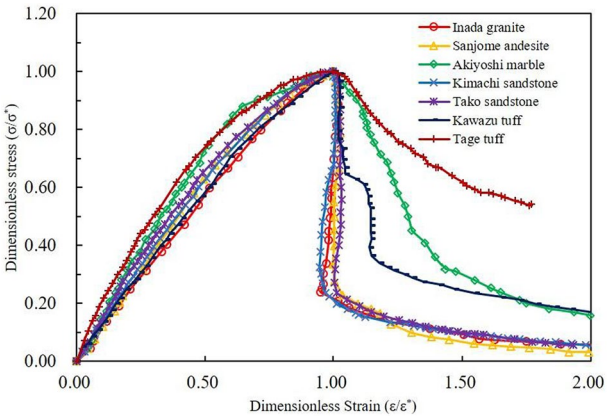

Fig. 1 Stress–strain curves of different rocks under the uniaxial direct tensile loading (experimental data from Okubo and Fukui 1996)

1 Introduction

Rock failure has been an area of active research for scientists for centuries, e.g., the classical hypotheses, including Coulomb's shear failure mechanism and Archimedes' tensile failure mechanism (Yu 2004; Meakin 1991). In recent years, many researchers have tended to believe that the macroscopic compression/shear failure of rock should be due to its tensile failure at a certain scale (Tang et al. 2005; Potyondy and Cundall 2004). In fact, the tensile failure of rock is crucial to many engineering practices. For example, catastrophic failures and instability in most rock engineering projects are usually caused by the tensile failure of rock, e.g., roof falls and rock bursts of underground caverns in hydraulic engineering. Moreover, the hydraulic fracturing technique that helps to extract underground resources out of ground mainly involves the tensile failure of rock as well. Researchers have conducted many experimental tests to investigate the mechanical responses of different rocks under tensile loading; such tests include direct tensile tests (Okubo and Fukui 1996) and indirect tensile tests (Li and Wong 2013). These works focus on the effect of various factors (e.g., the temperature and moisture content) on the uniaxial tensile strength of rock (Heuze 1983). The experimental results of Okubo and Fukui (1996) (see Fig. 1) show that there is a distinct post-peak response for the tensile failure of rock. Moreover, the post-peak behaviour of a material is important for energy consumption. For example, researchers in materials science have made super composites by adding glass fibres to composites to improve the post-peak properties (Hofmann et al. 2008). This concept has also been adopted in the field of rock engineering, e.g., researchers have modified the post-peak response of rock by adding rock bolts to enhance its energy absorption to prevent rock bursts (He and Zhao 2013).

In plasticity, the tensile response of rock (see Fig. 1) can be well-described using a model that includes strain hardening and strain softening. It can be easily described by a damage model, e.g., the damage coefficient can be directly obtained from the experimental curve. However, tensile failure is usually a localized failure (Barnhoorn et al. 2005) rather than a diffused failure. Because the deformation is concentrated in a narrow region and continuum mechanics might no longer be valid (Perić et al. 2014), caution must be taken when the damage and plastic model are used to describe the tensile failure of rock. Other concerns are the type of useful information that can be obtained from the experimental data of the tensile failure of rock and the method used to obtain it. In recent years, the mesoscopic numerical simulation has shown promise for use in further investigation and utilization of the experimental data of the tensile failure of rock (Wu et al. 2016; Yang 2015; Wang et al. 2016). For example, Wu et al. (2016) adopted the numerical manifold method (NMM) in conjunction with the cohesive zone model (CZM) to study rock failure and found that rock failure is related to the ratio between the normal stiffness and the shear stiffness. Yang et al. (2015) used the adhesive particle discrete element model (DEM) to analyse the crack initiation, propagation and convergence of the initial fractured red sandstone and concluded that the rock strength and elastic modulus would first increase and then decrease with the change in the initial crack angle. Wang et al. (2016) adopted the three-dimensional finite element model (FEM) combined with a mesoscopic stochastic damage model to study the effects of non-uniformity and other factors on the macroscopic tensile and acoustic emission properties. However, most previous works only focused on the influence of certain factors on the tensile failure responses of rock and did not explore the integration effect of the mesoscopic constitutive model, material heterogeneity, initial defect and model scale on the tensile failure of rock. In this work, this question will be investigated using the distinct lattice spring model (DLSM).

The lattice spring model (LSM) has shown great potential in the study of the failure and fracturing of materials (Hrennikoff 1941; Zhao 2017; Zhao et al. 2011). The main attractive point is that this type of method is able to provide insight into the macroscopic phenomena (the scale of specimen) through a physical-based simulation. For example, Zhao et al. (2014) studied the strain rate dependent of Sydney sandstone with the lattice spring model and found that the meso-structure (the scale of rock grain and pore) of rock could reproduce a strain rate effect of its dynamic tensile strength. The dynamic fracture energy increase mechanism of self-similar cracks with the crack length increasing has been successfully investigated using the lattice spring model. Using only Newton's second law and Hooke's law, the numerical simulation results reproduced the same observation with the experimental work and theoretical analysis. From the details of the energy distribution analysis, it is concluded that the redistribution of deformation energy derived from the similar crack propagation is an internal reason for the dynamic fracture energy increase (Zhao and Xia 2018). In this work, the DLSM is adopted to study the tensile failure of rock. First, the relationship between the dominant mesoscopic failure of rock, e.g., tensile or shear failure, along with its macroscopic tensile failure is studied. Second, the effects of mesoscopic geometries, such as the porosity, heterogeneity, and porous shape, on the tensile failure of rock are investigated. Third, the effects of macroscopic initial cracks/deflects are explored. Fourth, the influence of the mesoscopic constitutive relationship developed in this work and the model scale on the tensile failure of rock are studied. Finally, the method of utilizing tensile failure results of rock for parameters' selection of the mesoscopic constitutive model is established and verified against the available experimental results.

2 The Method

In the DLSM, as shown in Fig. 2, the rock is dispersed into a number of discrete particles linked by springs. The non-uniformity of rock is characterized by a texture-mapping approach, that is, by assigning different material properties to each particle to respond to the material heterogeneity (see Fig. 2b). Two particles are connected by a spring bond, which is comprised of a normal spring and a shear spring (see Fig. 2c). Different from the classical LSM, the DLSM adopts a multi-body shear spring to solve the Poisson's ratio limitation. The multi-body shear spring is realized by the shear deformation evaluation from the local strain of the particle cloud, which is formed by particles and their surrounding neighbours (see Fig. 2d).

In the DLSM, the rock failure is manifested as the breaking of a series of spring bonds. In this work, the mesoscopic

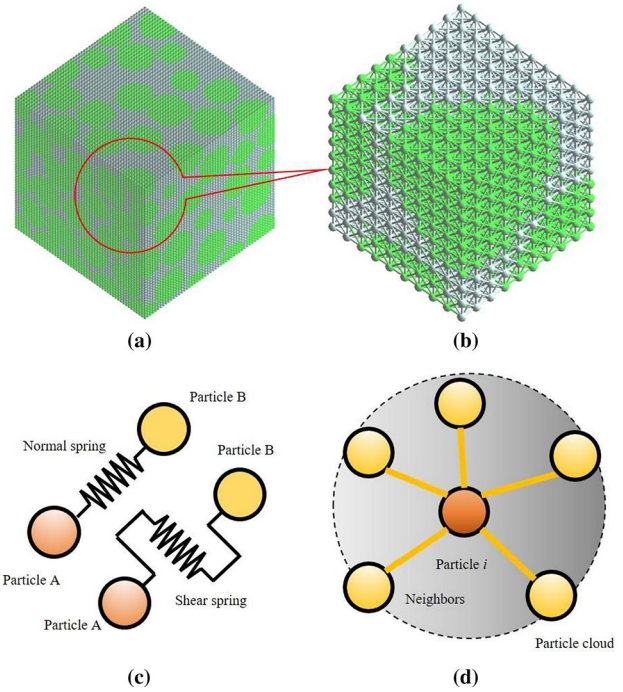

Fig. 2 Basic principles of the DLSM: **a** computational model characterization; **b** lattice spring structure; **c** normal and shear springs; **d** particle cloud for local strain calculation

damage model is further used to build up the constitutive model of the DLSM. The inter-particle interaction forces of the normal and shear springs are expressed as:

$$\mathbf{F}_{\mathrm{n},ij} = \left(1 - D\left(u_{\mathrm{n}}, u_{\mathrm{s}}\right)\right) k_{\mathrm{n}} \mathbf{u}_{\mathrm{n},ij} \tag{1}$$

$$\mathbf{F}_{\mathrm{s},ij} = \left(1 - D\left(u_{\mathrm{n}}, u_{\mathrm{s}}\right)\right) k_{\mathrm{s}} \mathbf{u}_{\mathrm{s},ij} \tag{2}$$

where $\mathbf{F}_{\mathrm{n},ij}$ and $\mathbf{F}_{\mathrm{s},ij}$ are the normal and shear interaction forces (vectors) between particles, respectively, $\mathbf{u}_{\mathrm{n},ij}$ and $\mathbf{u}_{\mathrm{s},ij}$ are the relative deformation vectors between particles, u_{n} and u_{s} are the normal and tangential deformations of the spring, respectively, $k_{\mathrm{n}}$and k_{s} are the shiftiness of the normal and shear spring, respectively, and $D\left(u_{\mathrm{n}}, u_{\mathrm{s}}\right)$ is the damage amount of the spring bond determined by the current deformation and its initial value is zero (refers to the intact spring).

Assume the normal spring satisfies the following damage function:

$$D_{\mathrm{n}}\left(u_{\mathrm{n}}\right) = \begin{cases} 0 & , \ u_{\mathrm{n}} < \alpha u_{\mathrm{n}}^{*} \\ f\left(\frac{u_{\mathrm{n}}}{u_{\mathrm{n}}^{*}}\right) & , \ u_{\mathrm{n}} < u_{\mathrm{n}}^{*} \\ 1 & , \ u_{\mathrm{n}} \geq u_{\mathrm{n}}^{*} \end{cases} \tag{3}$$

where u_{n}^{*} is the maximum tensile deformation of the spring and u_{n}^{*} is a dimensionless parameter to define the linear

elastic limit of the spring. The tensile parameter can be determined from a calibration process, which is to simulate the uniaxial tensile test and compare its result with the experimental result. The u_n^* is taken as the value when the difference between numerical and physical results is the minimum. When the elongation of the normal spring is greater than u_n^*, the spring is completely broken, that is, the amount of damage is set to 1. When the normal deformation is less than αu_n^*, the spring is in the elastic state. The damage in other ranges are determined by a damage function $f(\cdot)$. A similar model for the shear spring is introduced as:

$$D_s(u_s) = \begin{cases} 0 & , \ |u_s| < \alpha u_s^* \\ f\left(\frac{u_s}{u_s^*}\right) & , \ |u_s| < u_s^* \\ 1 & , \ |u_s| \geq \alpha u_s^* \end{cases} \tag{4}$$

where $|u_s|$ is the absolute value of the shear deformation, and u_s^* is the maximum shear deformation of the spring. For the shear deformation, there is no further distinction between the positive and negative signs during the calculation. However, for the normal deformation, the tension is defined as positive and the compression is defined as negative. In this work, the damage of the normal spring caused by compression is not considered. Under a given deformation state, the damage value of the spring bond between two particles can be given through the following formula:

$$D(u_n, u_s) = \max\left(D_n(u_n), D_s(u_s)\right), \tag{5}$$

when the cyclic loading/unloading is taken into account, the damage value of the bond is taken as the maximum historical damage value.

Through development of different damage functions, the DLSM can obtain different mesoscopic constitutive models. For example, according to the linear softening constitutive model, which is commonly used in the cohesive zone models (CZM) (e.g., Zhao and Xia 2018; Camacho and Ortiz 1996), the following damage function is given as:

$$f(x) = 1 - \frac{(1-x)\alpha}{x(1-\alpha)}, \tag{6}$$

where x corresponds to the non-dimensional spring deformation $x = u/u^*$ (u refers to the current deformation, and u^* refers to the ultimate deformation). This constitutive model corresponds to the damage function and is shown in Fig. 3. Note that the ratio between the post-peak region to the pre-peak region can be adjusted through the non-dimensional parameter α. When α is close to 1, the constitutive model turns into the original elastic–brittle constitutive model. The lower the α value is, the greater the post-peak region of the constitutive model and the closer the mesoscopic mechanical response to ductile failure.

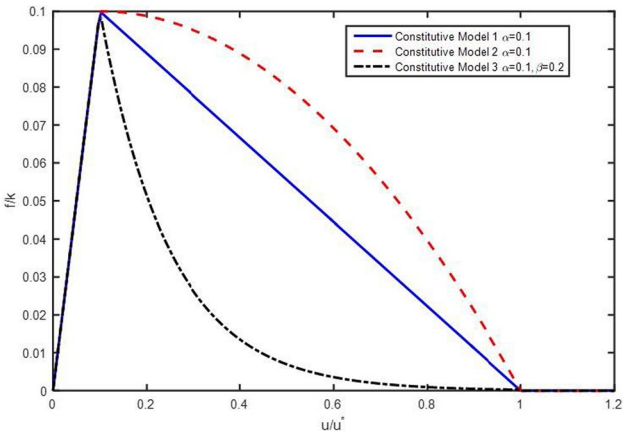

Fig. 3 Three mesoscopic constitutive models developed using different damage functions

Referring to the polynomial CZM model (Tvergaard 1990), the following polynomial damage function is proposed as:

$$f(x) = 1 - \left(1 - \left(\frac{x-\alpha}{1-\alpha}\right)^2\right)\left(\frac{\alpha}{x}\right). \tag{7}$$

This constitutive model is similar to the bilinear constitutive model. However, its post-peak region has a non-linear and upward convex characteristic (see Fig. 3).

According to the exponential form of the CZM model (Xu and Needleman 1994), the following exponential damage function is developed as:

$$f(x) = 1 - \left(\frac{\alpha}{x}\right)e^{\left(-\frac{x-\alpha}{\beta-\alpha/2}\right)}. \tag{8}$$

where β is a dimensionless parameter to control the shape of the constitutive model. Its constitutive curve has a concave post-peak region (see Fig. 3). When α is higher, the post-peak region will be truncated; when α is lower, the whole region will show the exponential curve post-failure, primarily with only a very short and steep linear curve for the pre-failure. The concavity of the specific curve can be adjusted by assigning different β values. When both the normal and shear springs are considered, the corresponding constitutive model for each spring bond can be represented by a three-dimensional surface (see Fig. 4). As an example, Fig. 4a shows the normal and shear spring constitutive model for the polynomial damage function, in which both the normal and shear damage are taken into account. When only the normal spring damage is considered, the corresponding constitutive model is shown in Fig. 4b. The coupling between the shear and normal deformations can break the shear spring as well. Figure 4c shows the normal and shear constitutive models, in which only the shear spring failure is considered.

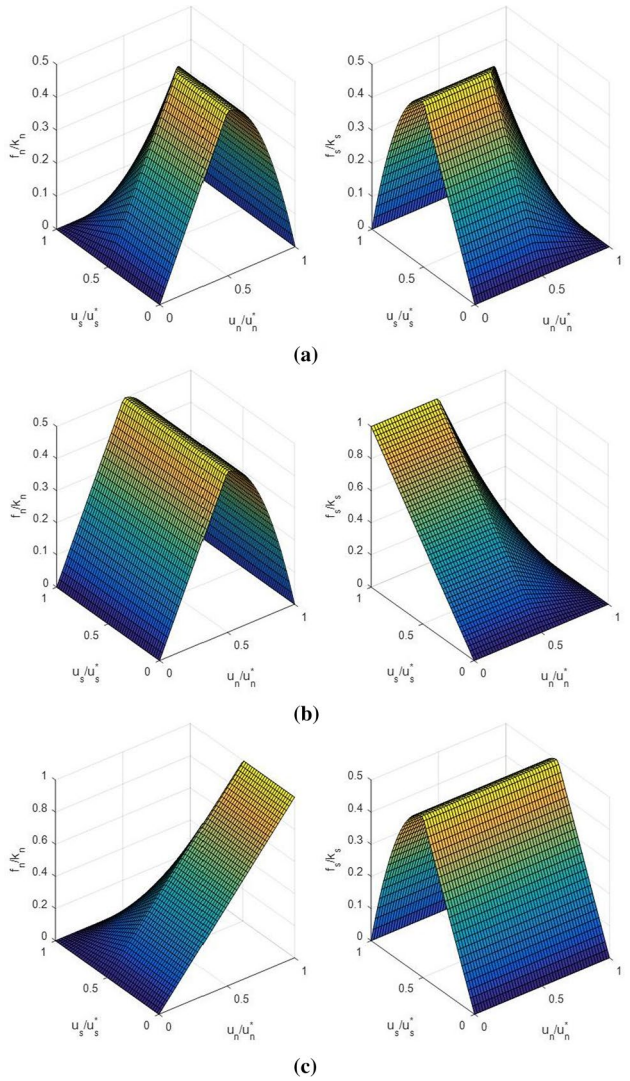

Fig. 4 3D surface of the constitutive model of normal and shear springs: **a** consider both normal and shear failures; **b** only consider the normal spring failure; **c** only consider the shear spring failure

The deformation of the normal spring in the DLSM is obtained from displacements of two particles:

$$u_{\mathrm{n}} = \left(\mathbf{u}_j - \mathbf{u}_i\right) \cdot \mathbf{n}, \tag{9}$$

where $\mathbf{u}_i$ and $\mathbf{u}_j$ are the displacements of two particles. $\mathbf{n}$ is the initial unit vector of the connected particles, which is obtained from initial positions of particles:

$$\mathbf{n} = \left(\frac{x_j - x_i}{\sqrt{\left(x_j - x_i\right)^2 + \left(y_j - y_i\right)^2 + \left(z_j - z_i\right)^2}}, \frac{y_j - y_i}{\sqrt{\left(x_j - x_i\right)^2 + \left(y_j - y_i\right)^2 + \left(z_j - z_i\right)^2}}, \frac{z_j - z_i}{\sqrt{\left(x_j - x_i\right)^2 + \left(y_j - y_i\right)^2 + \left(z_j - z_i\right)^2}} \right), \tag{10}$$

where x_i, y_i, z_i and x_j, y_j, z_j are the initial coordinates of the two particles.

The shear deformation between particles is obtained from the localized strain of two particles and is given as follows:

$$u_{\mathrm{s}} = \left\| [\boldsymbol{\varepsilon}]_{\mathrm{bond}} \cdot \mathbf{n}l - \left(\left([\boldsymbol{\varepsilon}]_{\mathrm{bond}} \cdot \mathbf{n}l \right) \cdot \mathbf{n} \right) \mathbf{n} \right\|. \tag{11}$$

The direction of the tangential deformation is given as follows:

$$\mathbf{n}_{\mathrm{s}} = \frac{[\boldsymbol{\varepsilon}]_{\mathrm{bond}} \cdot \mathbf{n}l - \left(\left([\boldsymbol{\varepsilon}]_{\mathrm{bond}} \cdot \mathbf{n}l \right) \cdot \mathbf{n} \right) \mathbf{n}}{\left\| [\boldsymbol{\varepsilon}]_{\mathrm{bond}} \cdot \mathbf{n}l - \left(\left([\boldsymbol{\varepsilon}]_{\mathrm{bond}} \cdot \mathbf{n}l \right) \cdot \mathbf{n} \right) \mathbf{n} \right\|}. \tag{12}$$

Under the given deformation, the interaction force between particles can be calculated through the constitutive function. Next, the particle force at the current time can be obtained through a summarization operation. Finally, the particle velocity can be updated based on Newton's second law:

$$\dot{\mathbf{u}}_i^{(t+\Delta/2)} = \dot{\mathbf{u}}_i^{(t-\Delta/2)} + \frac{\sum \mathbf{F}_j^{(t)}}{m_{\mathrm{p}}} \Delta t, \tag{13}$$

where m_{p} is the particle mass, and Δt is the time step. Those spring parameters k_{n} and k_{s} are obtained based on the input macroscopic elastic constants and the lattice's topological information:

$$k_{\mathrm{n}} = \frac{3E}{2\xi^{3\mathrm{D}}(1-2\upsilon)}, \tag{14}$$

$$k_{\mathrm{s}} = \frac{3(1-4\upsilon)E}{2\xi^{3\mathrm{D}}(1+\upsilon)(1-2\upsilon)}, \tag{15}$$

where E is the elastic modulus, υ is Poisson's ratio, and $\xi^{3\mathrm{D}}$ is the lattice coefficient that can be calculated by the following formula:

$$\xi^{3\mathrm{D}} = \frac{\sum l_i^2}{V}, \tag{16}$$

where l_i is the length of the spring bond in the lattice model and V is the represented macroscopic volume of the computational model.

3 Numerical Simulation

In this work, the displacement refers to the deformation of the specimen or spring bond. The strain refers to the engineering strain of the specimen.

3.1 Effect of the Mesoscopic Shear Failure

Under the uniaxial tension loading, the damage induced by both the shear and normal deformations could occur. The normal damage is supposed to be the dominant influence factor. However, the role of mesoscopic shear damage is still unclear. For example, the issue of whether pure shear damage could reproduce the macroscopic tensile failure and the corresponding macroscopic stress–strain relationship remain unclear. In this section, this issue will be addressed through a numerical uniaxial tensile test shown in Fig. 5.

In this test, the length of the specimen is 280 mm, the width is 75 mm, the thickness is 25 mm, the particle size is 1 mm, and the lattice configuration is the Cubic II configuration (see Fig. 5). There are 525,000 particles in the computational model. The elastic modulus of the specimen is 46.2 GPa, Poisson's ratio is 0.15, and the density is 2450 kg/m^3. A velocity loading is applied to both the top and bottom of the specimen to mimic the actual uniaxial tensile test. Here, the brittle constitutive model is adopted for the shear spring only, that is, the α parameter of the bilinear constitutive model is set to 1, in which the normal failure parameter u_n^* is set to 1 mm, and the shear failure parameter is set to 1.39×10^{-4} mm.

The numerical specimen will only involve the spring bond failure, which is induced by the shear deformation during the loading process. The progressive failure of the specimen during the test process is shown in Fig. 6a, in which red particles indicate that at least one of the linking springs of the particle has been broken, i.e., the damage value of the spring bond is 1. The specimen is first cracked at the loading end, and then this crack gradually expands from the end to the centre. During the damage propagation, due to the influence of the digital truncation error, the frontal surface of the damage is not symmetrical. Finally, the entire specimen reaches a complete failure state. However, from the stress strain curve in Fig. 6b, the specimen can still carry load, even if all particles are marked as broken. The reason for this result is that those springs that are only subjected to the tensile deformation remain undamaged, and the specimen does not lose its ability to continue to carry further tension loading. As shown in Fig. 6b, after the first peak has passed, the specimen enters a platform region, which corresponds to the expansion phase of the failure zone, and then the specimen enters the second loading phase. From this example, it can be concluded that the dominant mesoscopic controller of the uniaxial tensile failure is the failure of the normal spring rather than the shear

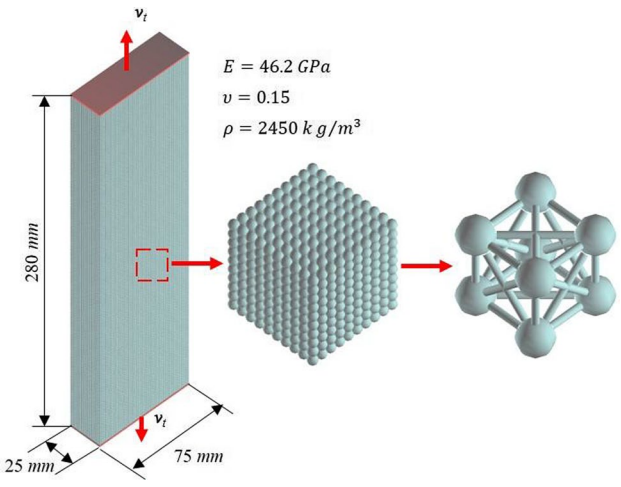

Fig. 5 The computational model settings and corresponding boundary conditions for the uniaxial tensile test

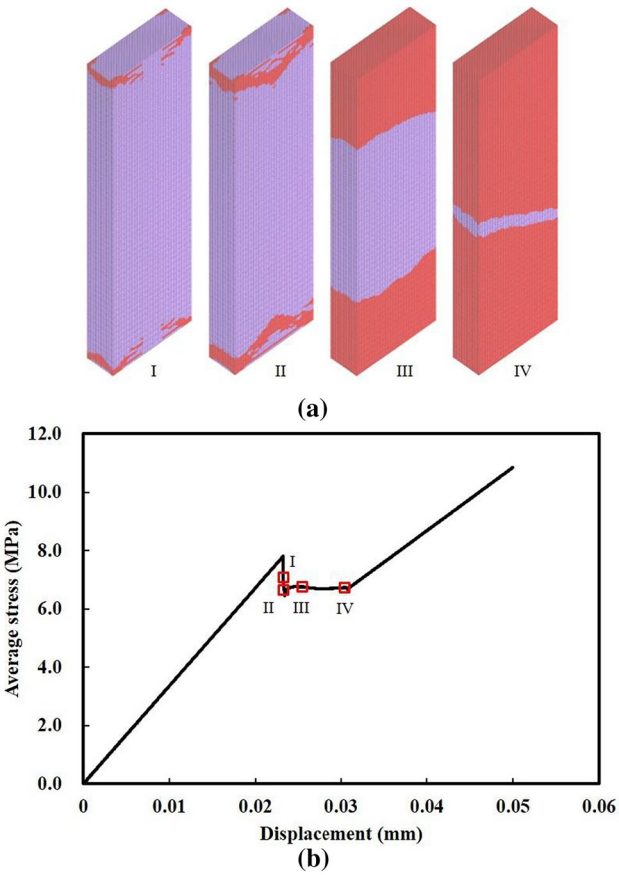

Fig. 6 Numerical simulation results with only considering the shear failure: **a** failure process; **b** displacement stress curve

spring. Therefore, this work will only focus on the influence of the normal spring.

3.2 Effect of the Loading Velocity

As an explicit numerical method, the DLSM adopts the minuscule time step to guarantee numerical stability; such a time step can result in a very long computational time of the quasi–static simulation. In the actual simulation, a higher loading velocity is used. Therefore, it is necessary to study the convergence of the computational results under different loading velocities. In this section, the computational model in Fig. 5 is further used to investigate the influence of the loading velocity. The same material parameters are adopted, except that the limit deformation u_{n}^{*} of the normal spring is set to 1.73×10^{-4} mm and the shear failure deformation is set to 1 mm. Thus, only the normal spring failure is considered.

Figure 7 shows the numerical simulation results at different loading velocities. At the low loading velocity, the specimen damage occurs at two ends. It is known that the velocity boundary condition would result in the applied surface to have zero deflection during the loading process. Therefore, it is a kind of rigid boundary condition and leads to a certain amount of stress concentration at the ends. The stress wave inside the specimen significantly fluctuates at high loading velocities; such a fluctuating stress wave becomes the dominant cause of the damage of the specimen, rather than the stress concentration. Therefore, when the loading velocity is high, multiple forms of damage will occur inside the specimen. This phenomenon can be further checked from the displacement stress curves of the specimen at different loading velocities. The loading curve exhibits a certain fluctuation characteristic at the high loading velocity.

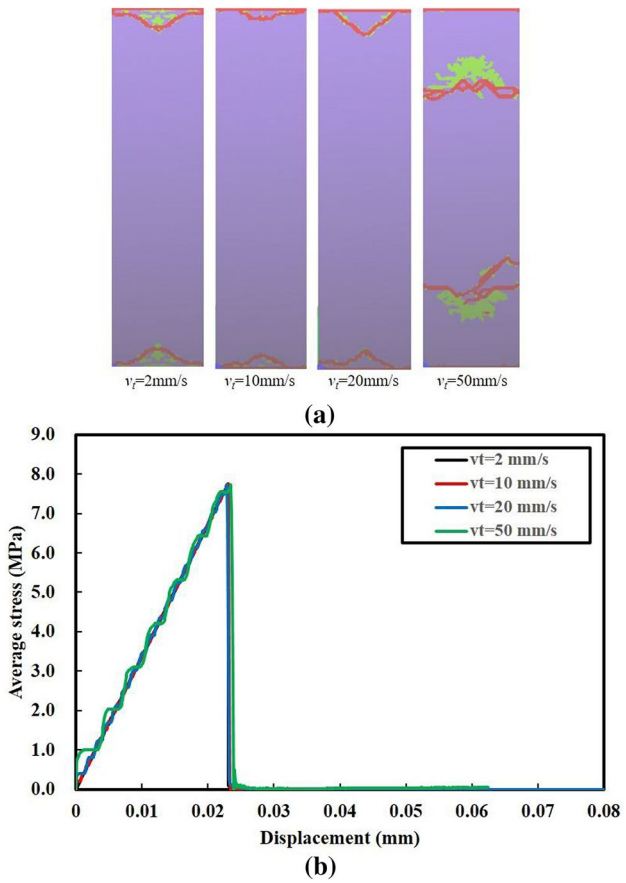

Fig. 7 Simulation results at different loading velocities: **a** failure patterns; **b** displacement stress curves

Note that a simple elasto-brittle constitutive relationship is used in this example. According to the limit deformation of the normal spring, the macroscopic tensile strength of this example can be predicted by the following formula:

$$\bar{\sigma}_t = E\frac{u_{\mathrm{n}}^{*}}{\bar{l}} = 8 \text{ MPa}, \tag{21}$$

where $\bar{l}$ is the mean length of the lattice spring and is set to 1 mm in this work. By observing the curves in Fig. 7b, it can be concluded that the macroscopic tensile strengths of the specimen at different loading velocities are all close to 8 MPa. This indicates that the damage of the specimen at the ends does not affect its macroscopic tensile strength. In the following simulations, 2 mm/s is set as the subsequent quasi–static loading velocity. The other conclusion in this section is that, when the mesoscopic constitutive model property is elastic–brittle, the corresponding macroscopic tensile response is elastic–brittle as well. It appears that there is no information lost between the macroscopic and mesoscopic constitutive reaction for the tension failure of the specimen. However, this conclusion is only conditionally correct, i.e., the brittle mesoscopic model will result in a brittle macroscopic response, whereas a macroscopic brittle response is not definitely induced from a mesoscopic brittle model. In the following sections, a deep investigation will be conducted.

3.3 Effect of the Non-uniformity

In this section, the influence of the non-uniformity of rock on the uniaxial tensile failure is considered. As shown in Fig. 8, three methods are used to consider the non-uniformity of rock. The first method is to construct a porous model by randomly removing a certain percentage of particles. Four models with porosities of 5%, 10%, 15%, and 20% are, respectively, generated. The second method is to construct a computational model with the higher porosity by randomly removing particles in a sphere, as shown in Fig. 8b. This model can correspond to sandstones and basalts with particularly high porosities. The third method is to set different

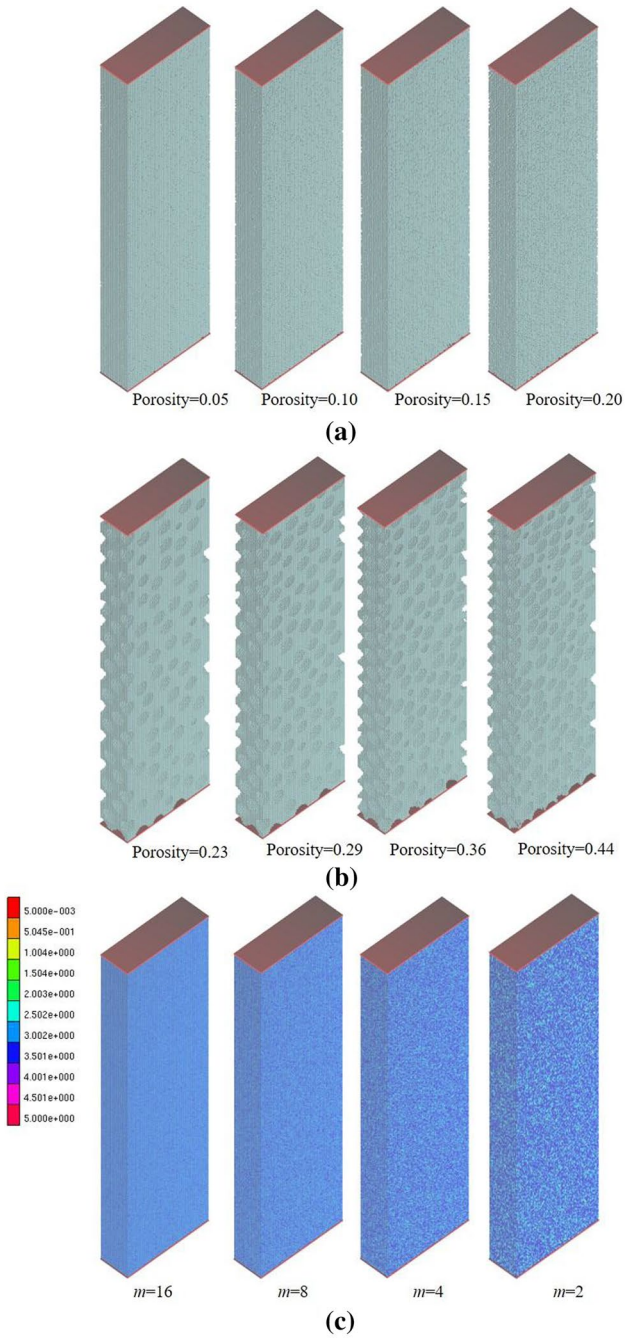

Fig. 8 Computational models with considering the non-uniformity: **a** the model with the porosity generated by random particle removal; **b** the model with different porosities generated by spherical pores; **c** the computational model with different m parameters (the strength parameter obeys the Weibull distribution, the higher the m value, the more uniform is the model)

strength reduction parameters for the spring bonds of the computational model and is realized through the following formula:

$$u^*_{\mathrm{n},ij} = \left(\zeta_i + \zeta_j\right) u^*_{\mathrm{n}}, \tag{22}$$

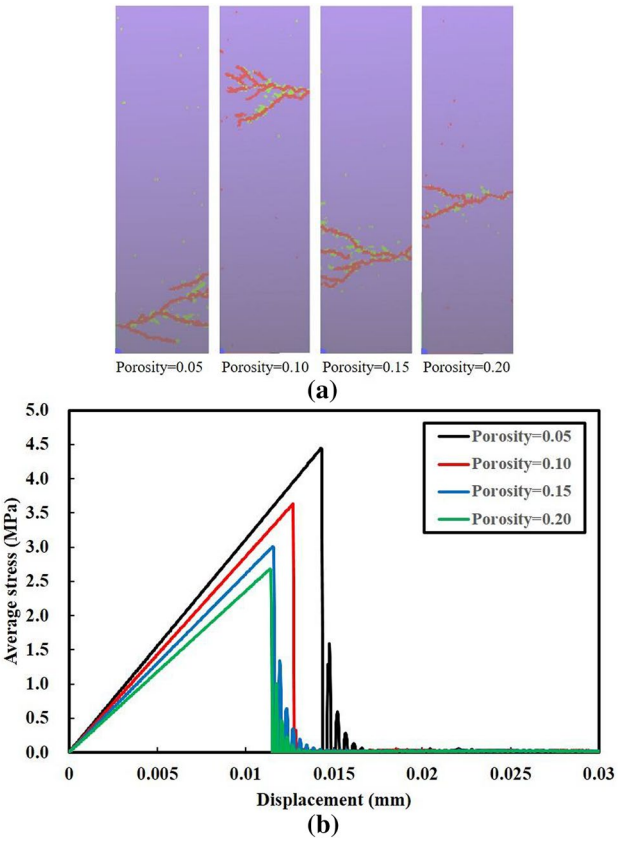

Fig. 9 Numerical simulation results of the DLSM with different random porosities: **a** failure patterns; **b** displacement stress curves

where ζ is a random number that satisfies a certain distribution. A single-parameter Weibull distribution function is used (the scale parameter is taken as 1):

$$f(\zeta) = m\zeta^{m-1}e^{-\zeta^m} \tag{23}$$

where m is a shape coefficient of the Weibull distribution, which could control the homogeneity of the specimen. Figure 8c shows the non-uniform models of the specimen using this approach. The colour of the particle represents the random number ζ corresponding to each particle. The greater the m value is, the more homogenous or uniform the specimen. This impression can be intuitively drawn from the colour distribution in the figure as well (see Fig. 8c). Other material parameters and boundary conditions are consistent with the computational model used in the previous sections.

Figure 9 shows the uniaxial tensile failures and stress–displacement curves of the computational models with random porosities using the first non-uniform model generation method. Figure 9a shows the failure patterns under different porosities. When the porosity is 5%, the tensile failure occurs at the lower end of the specimen, which is closer to the failure pattern in the actual experiment than the one in the pure homogenous model (see Fig. 7a); when the porosity

is 10%, the fracture exists at the upper end of the specimen, and a finger-like crack is exhibited; when the porosity is 15%, the fracture exists at the bottom of the specimen; finally, when the porosity is 20%, the fracture is exhibited at an intermediate position. Compared to the model with the lower porosity, when the porosity is 20%, the failure pattern consists of one main crack and two subcracks. Specimens with different porosities have different failure patterns. The reason for this is that the failure patterns are generated by the random removal of particles in the computational model, macroscopically reproducing different failure patterns.

Figure 9b shows the stress–displacement curves for each numerical specimen. The overall macroscopic elastic modulus decreases as the porosity increases, and the corresponding tensile strength decreases. For example, when the porosity is 5%, compared to the intact specimen, the strength is reduced approximately 3.5 MPa; when the porosity increases from 5 to 10%, there is a strength reduction of only 1 MPa. Therefore, the relationship between the porosity and macroscopic tensile strength is non-linear, especially at the beginning of the simulation. It is also concluded that the most effective method to make a stronger material is to reduce its voids (pores) to a certain small degree.

Figure 10 shows the uniaxial tensile failures as well as stress and displacement curves for the specimens with spherical porosities. Compared with the failure patterns of specimens generated by the first method, these specimens have fewer cracks. The red colour indicates that particles are broken and currently in the tension state, and the green colour indicates that particles are broken and currently in the compression state. The fracture pattern is close to the conventional experimental results of the uniaxial tensile tests of rock.

Figure 10b shows the corresponding stress and displacement curves. As the porosity increases, the corresponding macro-elastic modulus and strength will decrease. The magnitude of the change in the tensile strength is similar to these models generated by the first method (see Fig. 8b). The predicted macroscopic stress–displacement curves also have brittle characteristics, showing that random pores would not apparently affect the macroscopic tensile characteristic of rock.

Figure 11 shows the results taking into account the non-uniformity of the strength of the spring bond through the Weibull distribution. When m is equal to 16, the corresponding damage pattern of the specimen is finger-like, and the damage zone is at the bottom end of the specimen. This result is close to the one in the model with the low porosity (see Fig. 9a). When the value of m decreases, it will be closer to the single fracture failure of the specimen, and when the m value is equal to 2, the cracks will appear in two different parts of the specimen. From the stress–displacement curves, it is concluded that the corresponding tensile strength will

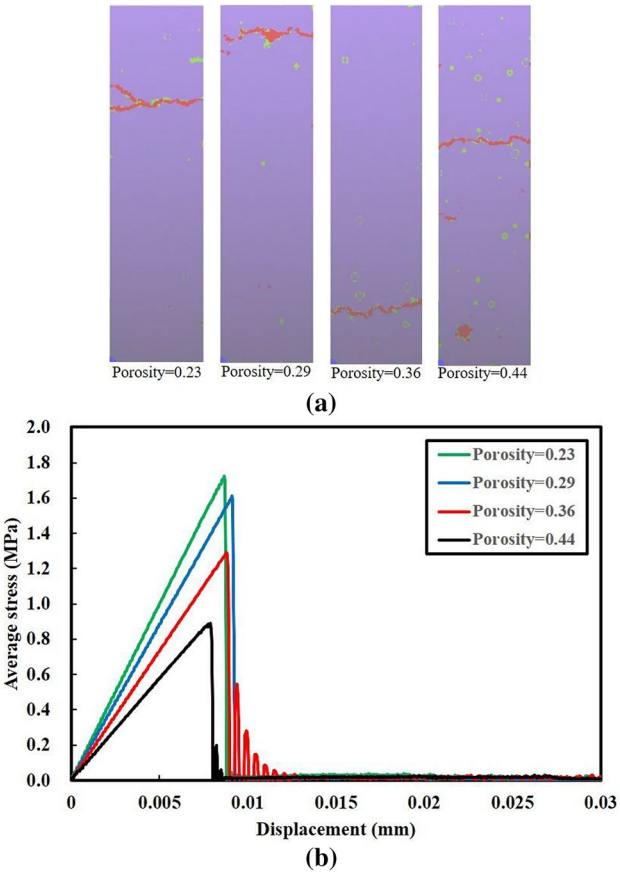

Fig. 10 Numerical simulation results of the DLSM with different porosities generated by spherical pores: **a** failure patterns; **b** displacement stress curves

increase with the increase in m value (homogeneity). Compared to the one in the random pore model, the corresponding elastic modulus does not change. The corresponding stress–displacement curves have a stronger non-linearity at the peak of the strength. Because the adopted spring model is brittle and there is a macroscopic non-linearity in the reproduced macroscopic response, it is indicated that the geometrical non-uniformity might result in the non-linearity of the macroscopic pre-failure stage of the tensile response of rock.

3.4 Effect of the Prefabricated Defect

Rock has a variety of complex internal defects and microcracks. In this section, the effect of these geometries on the tensile failure of rock will be investigated. As shown in Fig. 12, the specimen is prefabricated with two initial cracks. Different geometric structures are represented by setting different crack lengths. These prefabricated cracks are generated by removing particles from a given narrow area. The specific geometric parameters of each crack are

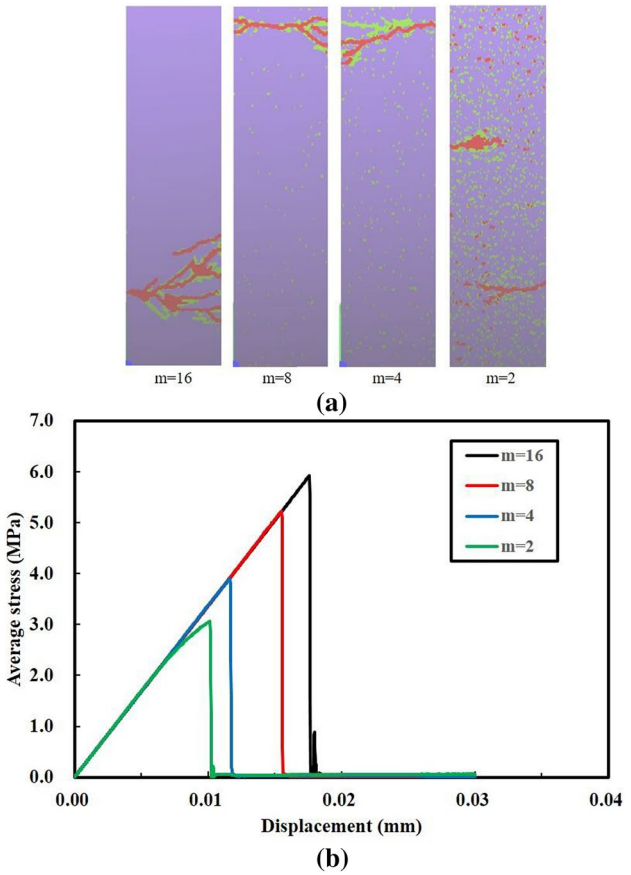

Fig. 11 Numerical simulation results of the DLSM with different *m* parameters of which the strength parameter of the spring bond obeys the Weibull distribution: **a** failure patterns; **b** displacement stress curves

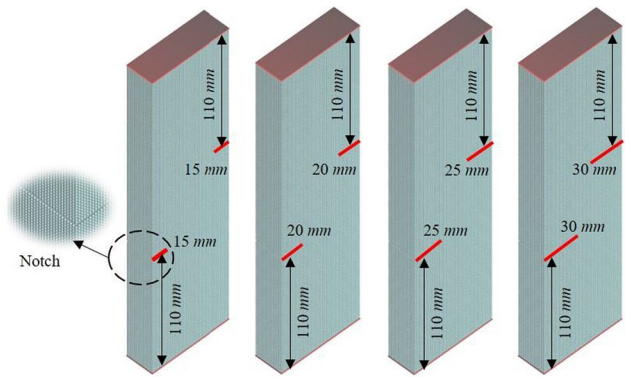

Fig. 12 Computational models with different prefabricated crack patterns

given in Fig. 12, and NL represents the initial crack length. The boundary conditions, material parameters, and loading rates of the specimen are the same with those in the previous sections. The corresponding numerical results are shown in Fig. 13. It is shown that the failure patterns of these specimens all expand along the prefabricated cracks. When NL is 15, there is a certain roughness corresponding to its fracture surfaces, and the lengths of its upper and lower fracture surfaces are different; this difference is caused by the asymmetry of the computational model and the digital truncation error. Figure 13b shows the stress–displacement curves of the specimen with different prefabricated cracks. As the length of the prefabricated crack increases, the macro-elastic modulus and tensile strength of the specimen will decrease, and the corresponding tensile strength will decrease as well.

Compared to the previous examples, the macroscopic response of this model shows obvious post-peak characteristics. Note that this model only considers the mesoscopic elasto-brittle constitutive structure, and the reproduced macroscopic response has an apparent post-peak portion. It is concluded that the prefabricated crack can lead to the post-peak tensile behaviour of rock, which might be the source of post-peak responses of some rock. However, it is difficult to represent the post-peak tensile behaviour by means of the prefabricated geometry in the actual simulation. For example, the quantitative control of the post-peak response (e.g.,

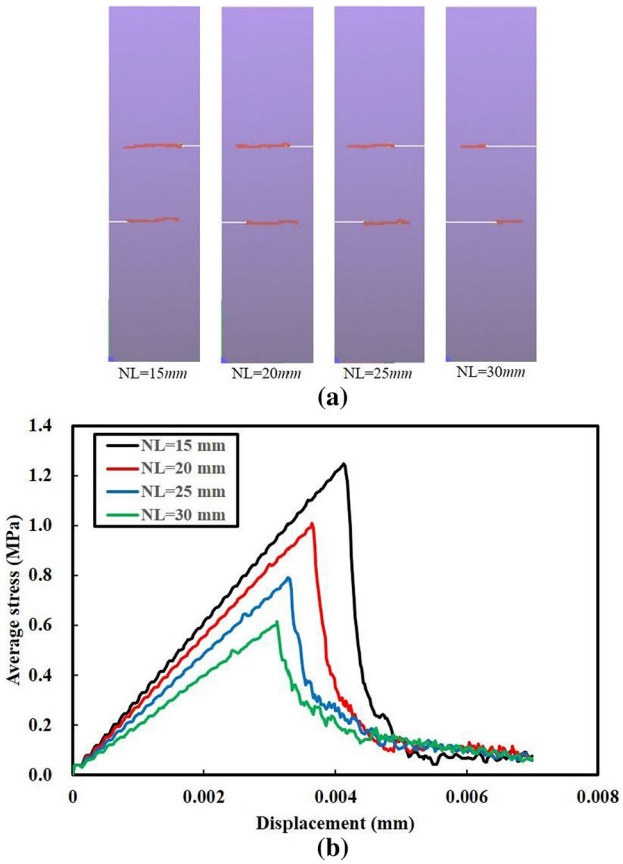

Fig. 13 Numerical simulation results of the DLSM with different prefabricated crack patterns: **a** failure patterns; **b** displacement stress curves

the slope) is difficult to be implemented. In addition, the geometric approach requires a large number of numerical units to be used, which further handicap its general application. Using the non-linear mesoscopic constitutive model is a viable solution. Adjusting parameters to control the tensile responses of rock has the advantages in terms of high computational efficiencies and ease of operations.

3.5 Effect of the Mesoscopic Constitutive Model

In this section, the influence of different constitutive models, e.g., the bilinear constitutive model, polynomial constitutive model, and exponential constitutive model, on the tensile failure characteristics of rock are investigated. The scale effect is first studied through the numerical simulation of uniaxial tensile tests with computational models of various lengths and is shown in Fig. 14.

The first computational model only considers two particles. The second model is a Cubic II unit, which is comprised of four particles. The other models are those that the lengths of the specimen are continuously increased by a multiple factor of 2 in the loading direction. This exponential increase is used to measure the changes in scale. The boundary conditions here are achieved by applying a tensile loading velocity at the top and bottom of the model. The material parameters are the same as those in the previous sections. The only difference is that the value of α, which corresponds to the constitutive model of the material, is set to 0.1.

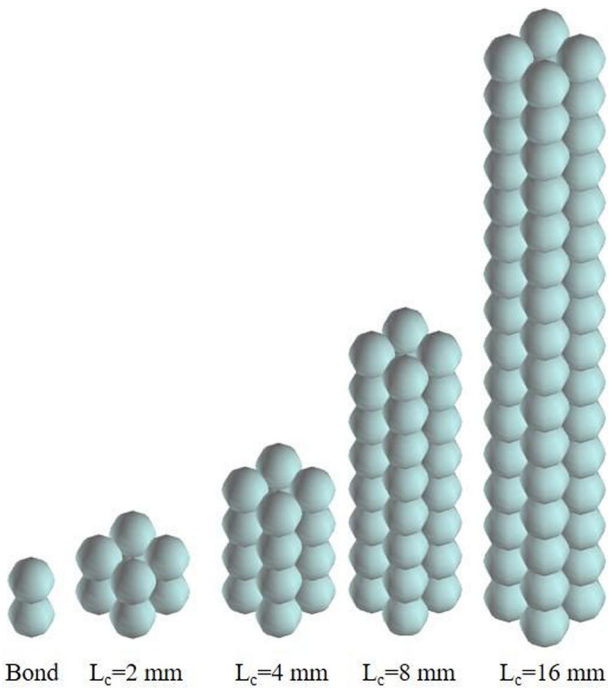

Fig. 14 Uniaxial tensile computational models with different lengths (applying the velocity loading at the top and bottom of the specimen)

Because the effect of the specimen scale (length) on the shape of the stress displacement curve is our primary concern, the results are normalized to for better comparison. The stress is divided by the tensile strength, and the strain is divided by the corresponding strain at the corresponding tensile peak. Figure 15a shows the corresponding results of the bilinear constitutive model. The tensile properties of the two-particle model correspond to the bilinear constitutive shape. For the Cubic II model, the corresponding tensile curve still has obvious post-peak characteristics. When approaching to the ultimate deformation, there are some fluctuations that might be caused by the lattice configuration of dialog connections. In addition, the pre-peak portion of the stress–displacement curve also shows a distinct non-linear characteristic. This non-linearity is caused by the post-peak portion of the bilinear constitutive model. When the length of the computational model is doubled, the post-peak portion will be drastically shortened. When the length of the specimen is further increased, the response of the model would exhibit obvious brittleness characteristics. Note that as the length of the specimen increases, the corresponding pre-peak non-linearity does not significantly change. Therefore, the change in the scale will have a significant effect on the post-peak portion of the tensile response of rock and a small effect on its pre-peak portion.

Figure 15b shows the stress–strain curves at different scales of the specimen for the polynomial constitutive model. The corresponding Cubic II model maintains the post-peak curve characteristics of the polynomial constitutive model. When L_c is 8 mm (8 particles) of the model, the corresponding post-peak portion is substantially reduced and has a consistent post-peak reduction as the bilinear constitutive model. Figure 15c shows the effect of the exponential constitutive model and the model scale on the tensile properties for $\alpha = 0.1,\ \beta = 0.2$. Unlike the first two constitutive models, the 8-particle length model will not show much information on its mesoscopic constitutive model. The effect of the polynomial and exponential constitutive models on the pre-peak portion of the tensile stress versus displacement curve is inconsistent with the bilinear constitutive model. It can be concluded from these results that an increase in the specimen length (scale) will cause the macroscopic tensile response to change from having a clear post-peak portion to being brittle-like. Therefore, directly extracting the post-peak response from the classical uniaxial tensile test with a brittle post peak is a difficult task. Nevertheless, the pre-peak non-linear response of the uniaxial tensile test might be a good source to determine whether a mesoscopic constitutive model with post-peak softening should be used or not.

To further study the influence of specific post-peak parameters of the mesoscopic constitutive models on the macroscopic tensile responses, a computational model is

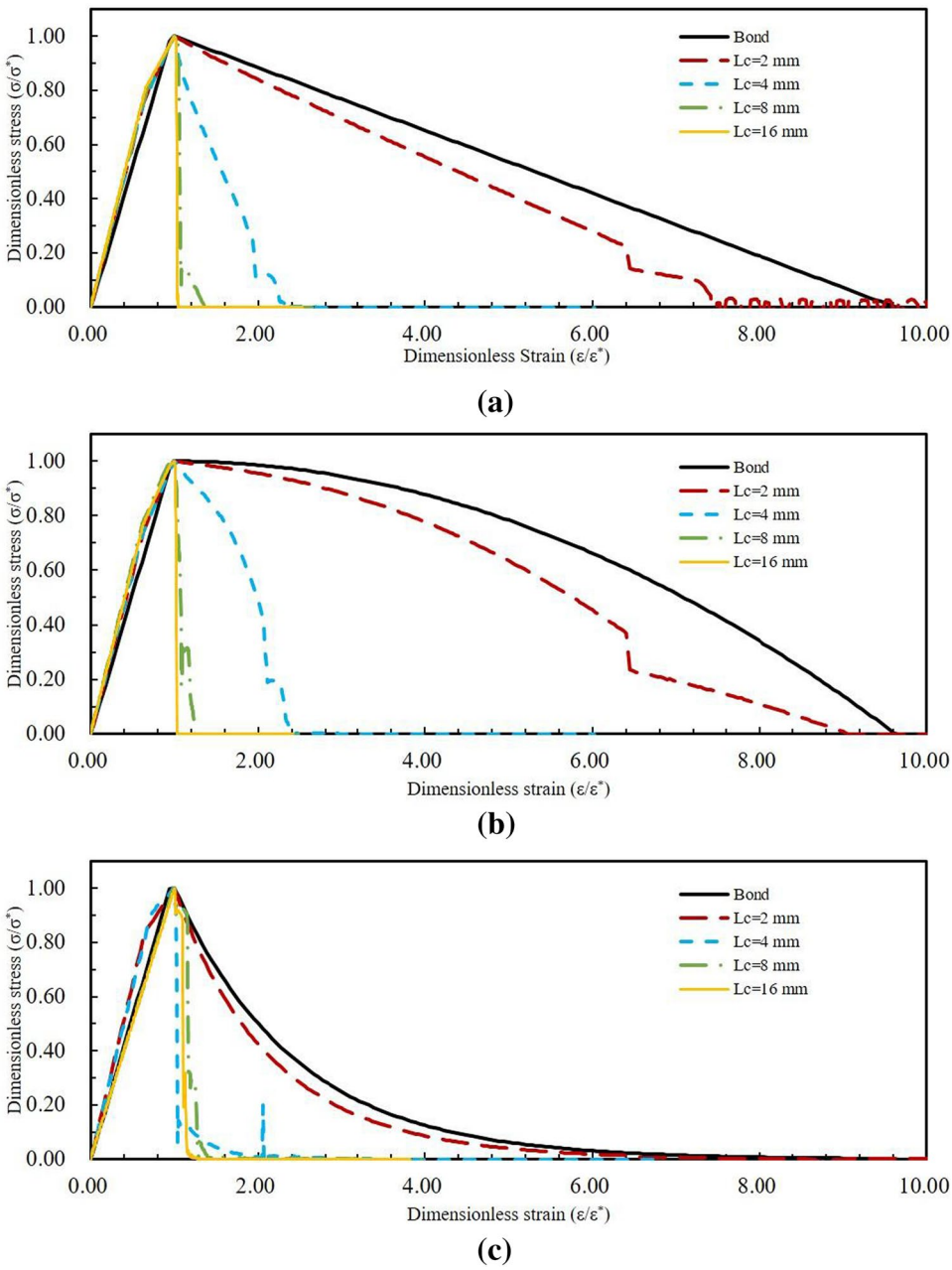

Fig. 15 Numerical results with considering different mesoscopic constitutive models and lengths of the specimen: **a** bilinear constitutive model; **b** polynomial constitutive model; **c** exponential constitutive model

built, as shown in Fig. 16. The difference between this model and the one shown in Fig. 14 is that the cross-section is extended to 10×10 particles. The loading conditions and material parameters are taken to be the same as those in the previous sections.

Figure 17 shows the normalized stress and displacement curves of different constitutive models. The macroscopic tensile mechanic curves of the bilinear constitutive are shown in Fig. 17a, in which the lower the α value is, the greater the post-peak portion. For example, $\alpha = 0.001$ indicates that the ratio of the pre-peak portion to the post-peak portion can reach 1000 times. The post-peak portion of the constitutive model changes with the change in α. As the post-peak portion of the mesoscale model is larger, the corresponding macroscopic stress curves have distinct post-peak portions, as well. However, for the bilinear model, a distinct post-peak response can only be obtained when the post-peak portion has a 100-fold ratio. Post-peak parameters have no significant effect on the non-linearity of the pre-peak portion, and a linear constitutive response only occurs when the constitutive model has the brittle characteristics, i.e., $\alpha = 0.0$. Polynomial constitutive models have similar effect on macroscopic tensile curves as well. The only difference is that the effect on the post-peak portion at $\alpha = 0.01$ is equivalent to the bilinear model of $\alpha = 0.05$. For the exponential constitutive model, when

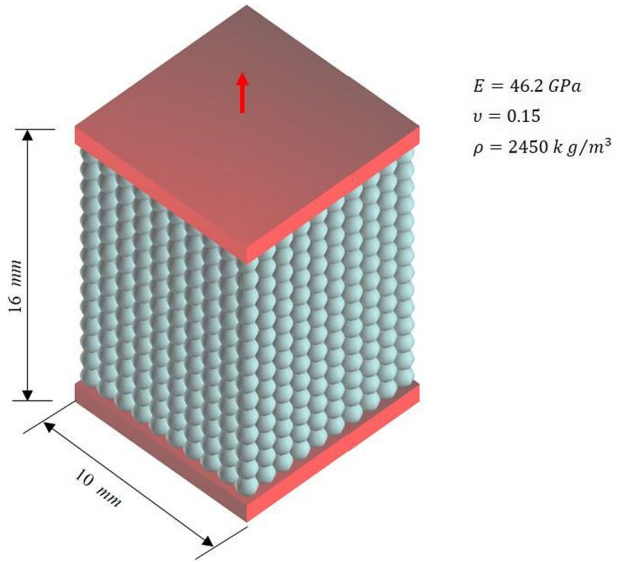

Fig. 16 The computational model with considering 10×10 particle cross-section for the uniaxial tensile test

α is low, the corresponding characteristics are related to only β. For the exponential constitutive model, α is fixed to 0.001, the corresponding macroscopic tensile curves for different values of β are shown in Fig. 17c. With the increase in β, the post-peak portion of the macroscopic tensile response will be more apparent.

Different post-peak parameters will affect not only the shape of the tensile curve but also the tensile strength. Figure 18 shows the effect of different constitutive parameters on the tensile strength. Figure 18a shows the relationship between the post-peak parameter α and the tensile strength for bilinear and polynomial constitutive models. The tensile strength here corresponds to the ratio of the tensile strength when the ultimate tensile deformation of the corresponding brittle constitutive model is αu_n^* and represents the increase in the macroscopic tensile strength caused by the post-peak portion of the mesoscopic constitutive model. From Fig. 18a, it can be concluded that, when the mesoscopic post-peak portion increases, the corresponding macro-tensile strength will increase. However, this increase has a certain upper limit of approximately 40%. When the post-peak parameters are low, the increase in the macroscopic tensile strengths in the post-peak portions of the bilinear constitutive and polynomial constitutive models has a certain difference. The polynomial constitutive model has a greater impact on the increase in the strength. When the post-peak portion is too large, the effects of these two constitutive models converge and become identical to each other. The response of the corresponding exponential constitutive model to the tensile strength is shown in Fig. 18b. With the increase in β, the post-peak portion expands and the tensile strength correspondingly increase. However, the ultimate increase in the corresponding macroscopic strength is approximately 30%.

The information in Fig. 18 can be used to select parameters in the actual numerical simulation of the tensile failure of rock. The tensile strength reproduced by the nonlinear constitutive model can be estimated by the following formula:

$$\sigma_t = \lambda \frac{u_n^*}{l} \alpha E, \tag{24}$$

where σ_t is the macroscopic tensile strength, and λ is a scale increase factor that can be assigned approximately between 1.3 and 1.5. To verify the above formula, a uniaxial tensile simulation of the model shown in Fig. 5 is performed, and the corresponding uniaxial tensile curves are shown in Fig. 19. It can be seen that it is possible to reproduce the post-peak response similar to the experimental tensile curves using different constitutive models. The post-peak behaviour can be used to further determine the selection of different constitutive models and the β value of the exponential constitutive model. The corresponding parameters of these three constitutive models are $u_n^* = 0.1$ mm and $\alpha = 0.001$, and the β value of the exponential constitutive model is 0.1. The calculated tensile strength of the corresponding three constitutive models is 6.7 MPa, and the value obtained by Formula (24) is from 6.0 to 6.9 MPa. Therefore, Formula (24) is feasible.

4 Conclusion

The distinct lattice spring model (DLSM) is used in this paper to investigate the tensile failure of rock. To study the effect of the meso-constitutive structure, three non-linear constitutive models are further developed. The effects of the geometric heterogeneity of rock, mesoscopic constitutive model, and model scale, on the pre-peak and post-peak characteristics of the macroscopic tensile responses of rock are fully investigated. To study the geometric heterogeneity of rock, numerical tests are conducted by introducing the random geometric structures, macroscopic fracture structures, and random non-uniformity of the strength parameters.

Through numerical simulation, a few conclusions are drawn. First, shear spring failure does not control the macroscopic tensile failure. Therefore, the macroscopic tensile experimental curves rather than the shear ones mainly carry the mesoscopic tensile failure information. Second, the material non-uniformity in terms of random porosity distribution and random distribution of the strength of the material units could reproduce the pre-peak non-linear responses of rock. It is only possible to reproduce the

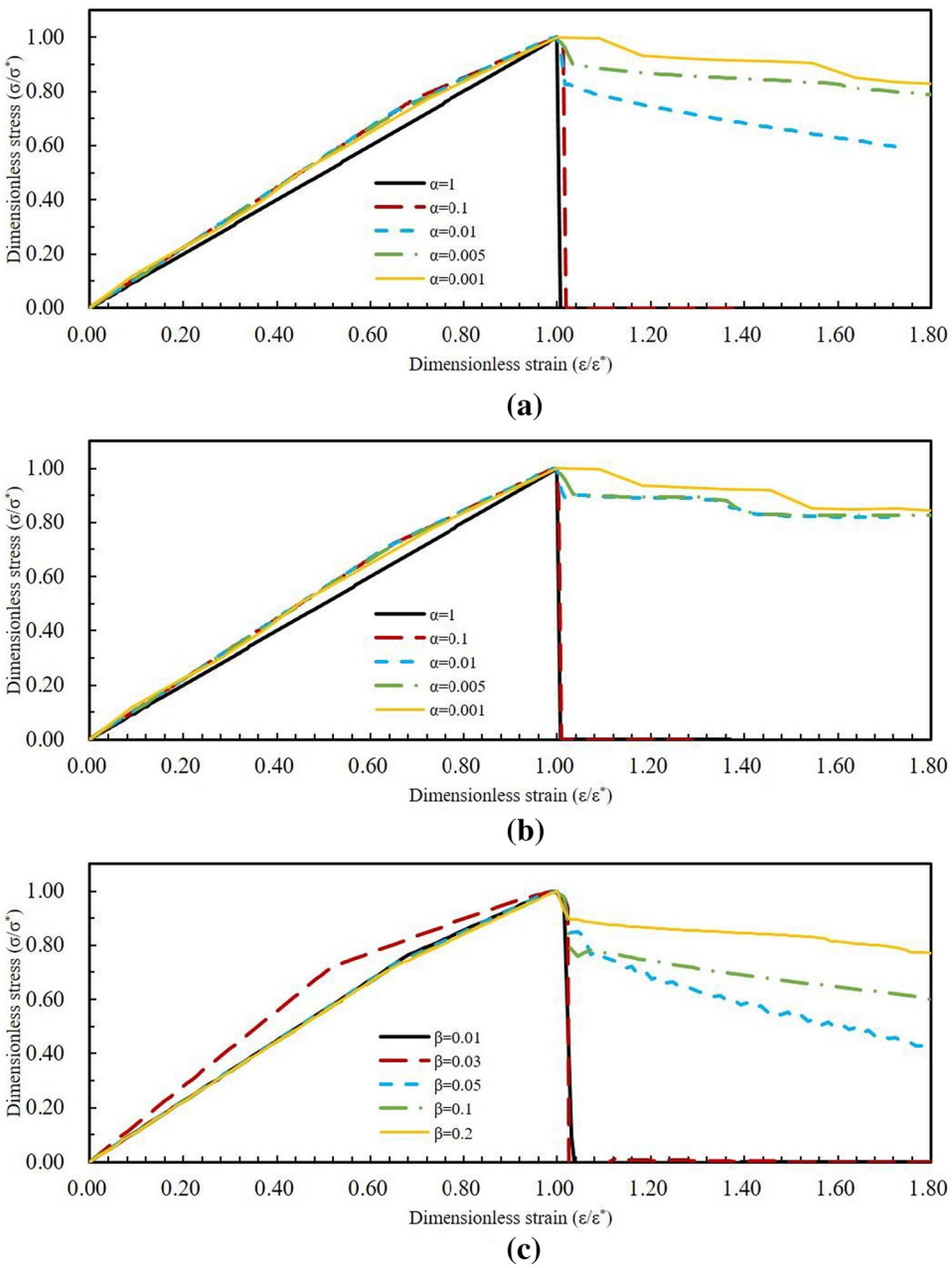

Fig. 17 The relationships between constitutive parameters and tensile stress–strain curve morphologies for different constitutive models: **a** bilinear constitutive model; **b** polynomial constitutive model; **c** exponential constitutive model ($\alpha = 0.001$)

post-peak response through setting macroscopic defects. Finally, this reveals that the nature of the pre-peak and post-peak characteristics of the tensile behaviour of rock can be reproduced from purely geometric effects using a simple brittle constitutive model.

The effect of the mesoscopic constitutive models and the scale effect were also considered. The scale affects both the post-peak region (make it brittle) and the strength (make it stronger). The post-peak non-linearity of the mesoscopic constitutive model will influence both the pre-peak and post-peak responses of rock, although the influence on the pre-peak portion is independent of the scale. However, this type of influence on the post-peak portion is scale dependent. An empirical formula considering the scale influence and the post-peak parameters of the constitutive model is established and can be used to determine the corresponding mesoscopic parameters in modelling the tensile failure of rock.

The tensile failure is commonly encountered in most rock engineering projects, e.g., rock roof falls and rock bursts of underground caverns. The results of this study might provide some ideas to model these tensile failure problems in actual rock engineering practices more rationally. For example, due to the computational limitation, the numerical element size in the actual modelling of rock engineering is usually in the order of a few meters. Through investigation, this study

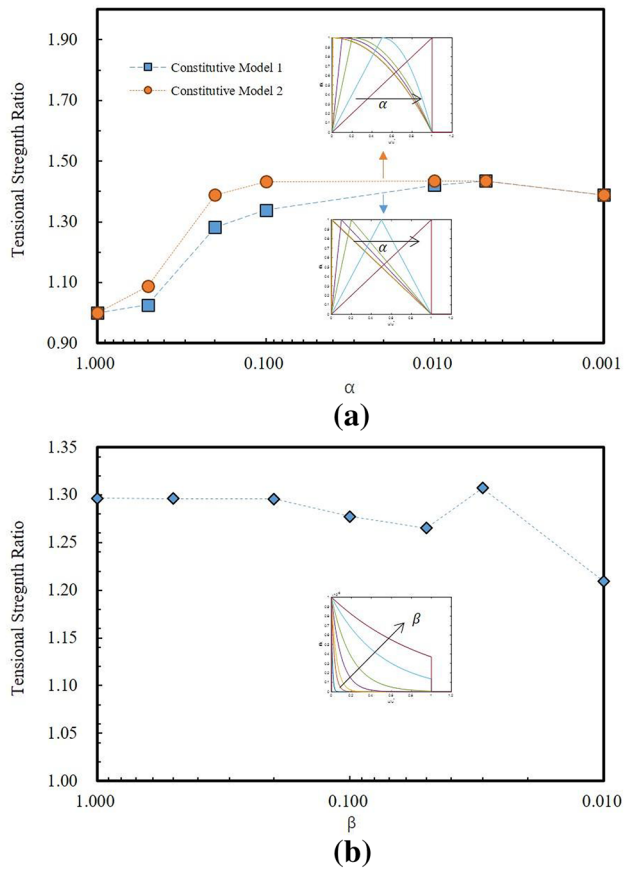

Fig. 18 The relationships between constitutive parameters and the macroscopic tensile strengths: **a** bilinear and polynomial constitutive models (constitutive models 1 and 2); **b** exponential constitutive model (constitutive model 3, $\alpha = 0.001$)

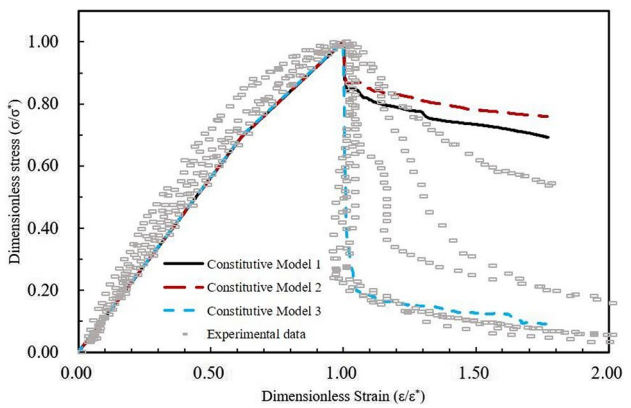

Fig. 19 The stress–strain curve morphologies of the 280 mm-long computational model (see Fig. 5) using different constitutive models (constitutive model 1, 2 and 3 refers to the bilinear, polynomial and exponential constitutive models, respectively)

reveals that a simple brittle constitutive model could be used, even if the tensile behaviour of the rock specimen shows the obvious post-peak response, the only change is that the tensile strength should be set as 1.3–1.5 times as the experimental value.

Acknowledgements This research is financially supported by the National Key Research and Development Program of China (2016YFC0401900), National Natural Science Foundation of China (U1765202, 1177020290) and Program of Introducing Talents of Discipline to Universities (B14012).

References

Barnhoorn A, Bystricky M, Kunze K, Burlini L, Burg JP (2005) Strain localisation in bimineralic rocks: experimental deformation of synthetic calcite–anhydrite aggregates. Earth Planet Sci Lett 240(3):748–763

Camacho GT, Ortiz M (1996) Computational modelling of impact damage in brittle materials. Int J Solids Struct 33(20–22):2899–2938

Christensen RM (2016) Perspective on materials failure theory and applications. J Appl Mech 2016:83

Espinosa HD, Zavattieri PD (2003) A grain level model for the study of failure initiation and evolution in polycrystalline brittle materials. Part II: numerical examples. Mech Mater 35(3–6):365–394

He M, Zhao F (2013) Laboratory study of unloading rate effects on rockburst. Disaster Adv 6(9):11–18

Heuze FE (1983) High-temperature mechanical, physical and thermal properties of granitic rocks—a review. Int J Rock Mech Min 20(1):3–10

Hofmann DC, Suh JY, Wiest A et al (2008) Designing metallic glass matrix composites with high toughness and tensile ductility. Nature 451(7182):1085–1089

Hrennikoff A (1941) Solution of problems of elasticity by the framework method. ASME J Appl Mech 1941:A619-A715

Li D, Wong LNY (2013) The Brazilian disc test for rock mechanics applications: review and new insights. Rock Mech Rock Eng 46(2):269–287

Meakin P (1991) Models for material failure and deformation. Science 252(5003):226

Okubo S, Fukui K (1996) Complete stress-strain curves for various rock types in uniaxial tension. Int J Rock Mech Min 33(6):549–556

Perić D, Zhao G, Khalili N (2014) Strain localization in unsaturated elastic-plastic materials subjected to plane strain compression. J Eng Mech 140(7):04014050

Potyondy DO, Cundall PA (2004) A bonded-particle model for rock. Int J Rock Mech Min 41(8):1329–1364

Tang CA, Wong RHC, Chau KT, Lin P (2005) Modeling of compression-induced splitting failure in heterogeneous brittle porous solids. Eng Fract Mech 72(4):597–615

Tvergaard V (1990) Effect of fibre debonding in a whisker-reinforced metal. Mater Sci Eng A 125(2):203–213

Wang SY, Sloan SW, Sheng DC, Tang CA (2016) 3D numerical analysis of crack propagation of heterogeneous notched rock under uniaxial tension. Tectonophysics s 677–678:45–67

Wu Z, Fan L, Liu Q et al (2016) Micro-mechanical modeling of the macro-mechanical response and fracture behavior of rock using the numerical manifold method. Eng Geol 225:49

Xu XP, Needleman A (1994) Numerical simulations of fast crack growth in brittle solids. J Mech Phys Solids 42(9):1397–1434

Yang SQ (2015) Discrete element modeling on fracture coalescence behavior of red sandstone containing two unparallel fissures. Eng Geol 178(6):28–48

Yu MH (2004) Advances in strength theories for materials under complex stress state in the 20th century. Adv Mech 34(4):529–560

Zhao GF (2017) Developing a four-dimensional lattice spring model for mechanical responses of solids. Comput Meth Appl Mech Eng 315:881–895

Zhao GF, Xia KW (2018) A study of mode-I self-similar dynamic crack propagation using a lattice spring model. Comput Geotech 96:215–225

Zhao G, Fang J, Zhao J (2011) A 3D distinct lattice spring model for elasticity and dynamic failure. Int J Numer Anal Methods Geomech 35(8):859–885

Zhao GF, Russell AR, Zhao X, Khalili N (2014) Strain rate dependency of uniaxial tensile strength in gosford sandstone by the distinct lattice spring model with X-ray micro CT. Int J Solids Struct 51(7–8):1587–1600